Highly Efficient Solar Energy Harvesting in Phosphorene-Graphene Quantum Dot van der Waals Heterostructures: An Ab-initio Approach

W. M. Uvin G. De Alwis, K. L. Dimuthu M. Weerawardene and Kevin L. Shuford*

Department of Chemistry and Biochemistry, Baylor University, One Bear Place #97348, Waco,
TX 76798-7348, USA

* Kevin_Shuford@baylor.edu, 1-254-710-2576, fax : 1-254-710-4272

ABSTRACT

This study delves into the intricacies of creating highly effective power conversion assemblies from van der Waals heterostructures of phosphorene and graphene quantum dots by employing density functional theory calculations. We emphasize the role of individual monomer properties and their interlayer interactions on the power conversion ability by focusing on visible light absorption, charge carrier generation and their separation. Different edge atom functionalization (H, NH_2, Cl, OCN, CN) in the phosphorene quantum dots and heteroatom doping (Group IV = Si, Ge, and Group VI = O, S, Se) in the basal plane of graphene quantum dots were employed to alter the monomer properties. Our results indicate that select combinations of these modification techniques yield staggered frontier molecular orbital alignments (Type II) with spatial separation of the highest occupied and lowest unoccupied molecular orbitals. These candidates possess improved visible light absorption range with reduced intensities owing to the dominance of charge transfer excitations. Edge functionalization of phosphorene was identified as the most significant contributor to interlayer interaction strength, with functional groups that are electron-withdrawing in nature forming stronger interactions. Heteroatom doping of graphene was recognized as the most important contributor to improving visible light absorbance owing to the reduction in fundamental gaps. From the candidates considered, systems with relatively weaker interlayer interactions were determined to be better at charge carrier separation due to the potential gradient being concentrated at the interfacial region. These systems possess approximated power conversion efficiencies ranging between 11-29%, amongst the highest reported for quantum dot systems characterized by density functional theory calculations.

1. INTRODUCTION

The need for a robust approach to utilizing renewable energy as a viable alternative to declining reserves of fossil fuel is at an all-time high.[1] To this extent, the focus has been on effectively harnessing solar energy, highlighting the necessity of effective power conversion devices that transform solar energy into electrical current (photovoltaics) or chemical energy (photocatalysis). Thus, focusing on novel nano-scale materials, also known as low-dimensional materials, with high solar light absorption, charge-carrier generation, and charge separation capabilities is imperative.

Low-dimensional materials, colloquially used as an umbrella term to refer to two-dimensional (2D),[2] one-dimensional nanowire,[3] or zero-dimensional quantum dot (QD) materials,[4] have garnered a lot of attention owing to their robust and tunable electronic, optical, mechanical, and thermal properties that result from high surface area to volume ratios and quantum confinement. The exfoliation of graphene by Novoselov et al. in 2004[5, 6] led to the development of other 2D materials like phosphorene,[7] transition metal dichalcogenides,[8] graphitic carbon nitride (g-C_3N_4),[9] hexagonal boron nitride,[10] perovskites,[11] and MXenes,[12] which prompted investigations into constraining the dimensionality even further. Different monomer modification techniques like dimensionality control, composition tuning (doping, alloying, functionalization), and inclusion of external fields (electric fields or strain fields) are used to alter material properties.[13]

A more intriguing approach to tuning system properties is the formation of heterostructures, where two or more materials are combined. The central challenge here is to retain surface properties or modulate them in a controlled manner without introducing unwanted electronic states.[14] The traditional prescription for heterostructure formation has been covalent bonding between constituent materials. However, this approach requires akin lattice and electronic structures, as even a slight mismatch could lead to defects/dislocations that can propagate beyond the interface,[15] leading to uncontrollable Schottky barriers, Fermi level pinning, and undesired interfacial trapping states that hinder device performance.[16,17] An alternate way to integrate materials is the formation of heterostructures utilizing the relatively weak van der Waals (vdW) interaction,[18] which generally encompasses dipole-dipole, dipole-induced-dipole, and induced dipole-induced dipole interactions but is broadly used to characterize all composite assemblies that are typically stacked vertically via non-bonding interactions.[19] This method offers a higher degree of flexibility in its ability to combine dissimilar materials, giving rise to an additive effect of electronic properties,[20] which can be modulated by the electronic hybridization of neighboring layers based on the amount of energy and momentum overlap.[21] These composite systems are stable, with in-plane covalent bonds within each material, while the relatively weak non-bonding forces are generally sufficient to overcome gravitational forces for most nanoscale and macroscale materials.

vdW systems are particularly advantageous for photocatalytic and photovoltaic applications, as the electronic hybridization between layers can be used to tune interlayer, intralayer, and hybrid excitons, thereby enabling the composite system to achieve a desired balance between light absorption capabilities and spatial separation of charge carriers. Theoretical investigations revealed that 2D vdW heterostructures of blue-phosphorene/boron-arsenide[22], CdS/C_2N, CdSe/C_2N[23], GeS/MoS_2, GeSe/MoS_2, SnS/MoS_2[24] are potential candidates for the water splitting reaction owing to the individual band edge energetics and formation of type-II-like staggered band alignment, which can promote interlayer or hybrid excitons. Similarly, graphene/MoS_2,[25] MoS_2/$MoSe_2$,[26] MoS_2/g-C_3N_4,[27] and phosphorene/MoS_2[28] are a few examples of 2D material combinations investigated in the construction of vdW heterostructures as potential solar cell materials. Additionally, other lower dimensional forms of edge-modified phosphorene nanoribbon heterostructures,[29] edge-modified phosphorene nanoflake heterostructures,[30] edge-modified phosphorene antidot heterostructures,[31] and finite graphene, silicene, and arsenene heterostructures[32] were shown to achieve desirable power conversion efficiencies and charge carrier separation through theoretical investigations. Apart from material choice, electric fields,[33,34] twist angles,[35] pressure[36] , and strain[37] can be used as knobs to tune the absorption and lifetimes of these interlayer, intralayer, and hybrid excitons.

The formation of vertically-stacked vdW heterostructures has also been explored as a means to encapsulate material surfaces, thereby preventing subsequent degradation while maintaining the parent material properties as demonstrated with 2D phosphorene and graphene[38, 39,40,41,42] and Al_2O_3 coating on phosphorene.[43] Due to its excellent electronic,[44] optical,[45] mechanical,[46] and thermal properties,[47] phosphorene, an elemental 2D material with sp^3 hybridized phosphorous atoms and an anisotropic geometry, is a viable candidate for visible-light-driven energy conversion applications.[48] The limiting factor in phosphorene has always been its ambient stability,[49] which has been shown to improve upon encapsulation by employing materials like graphene via vdW interactions.

In this work, we focus on a relatively underexplored realm of designing quantum dot van der Waals heterostructures by incorporating edge-functionalized, phosphorene quantum dots (PQDs) with graphene quantum dots (GQDs) to form composite assemblies that could be used in visible light-driven energy conversion applications. An advantage of using quantum dot candidates is their discrete, molecular-like energy levels that promote exciton generation at varied frequencies, thereby reducing thermalization losses and mimicking the performance characteristics of multi-junction semiconducting devices. The motivation to use GQDs was driven by their capacity to enhance the ambient stability of phosphorene while also largely preserving the individual electronic properties of the composite system. To this end, we employ density functional theory computations to investigate the viability of these QD-vdW heterostructure systems as power conversion devices. We modulate the individual QDs by changing the edge terminating group on the PQDs and doping the basal plane of GQDs with group IV or Group VI heteroatoms. This work aims to decipher the effect of these tuning mechanisms in enhancing visible light-driven energy conversion in the context of these QD-vdW heterostructure systems while shedding light on the role of interlayer interactions and their strength in power conversion applications.

2. METHODS

The hexagonal $C_{54}H_{18}$ GQD with six zigzag edges, based on the experimentally available Circumcoronene[50] framework, has been selected as a potential donor candidate in this study. This particular GQD has also been widely used in other theoretical studies to model GQDs with hydrogen functionalization at the edges.[51,52,53] Additionally, we have explored heteroatom doping of Group IV and Group VI elements (Si, Ge, O, S, Se) in the basal plane of GQDs as a technique to modulate the donor candidate's electronic and optical properties. Edge-functionalized rectangular PQDs, denoted as $P_{56}X_{22}$, consisting of 56 phosphorus atoms and 22 edge sites have been employed as a potential acceptor material. The utilization of the P_{56} backbone in this investigation was driven by its similarity in size to the GQD and the minimal edge state contributions to the frontier molecular orbitals, as evidenced in our previous work.[54] Here, we have used different edge functional groups (H, NH_2, Cl, OCN, CN) based on our previous work[45, 54] as a modulation technique to probe the optoelectronic properties of the acceptor while passivating the edge sites. Including the pristine GQD, we have six donor and five acceptor candidates, giving us 30 heterostructure assemblies for consideration.

Electronic, optical, and geometric properties of all monomer and heterostructure systems were obtained upon performing full geometry optimizations with Becke 3-parameter Lee-Yang-Parr (B3LYP) global hybrid density functional[55, 56] in conjunction with a Pople-type split valence, triple-ζbasis set (i.e., 6-311g(d,p)) with polarization functions (d orbitals on nonhydrogen atoms and p orbitals on hydrogen atoms). Grimme's dispersion corrections (DFT+D3)[57] were employed to account for the interlayer vdW interactions. The dispersion corrections were also applied to the monomer units to ensure uniformity across calculations. Harmonic vibrational frequencies were obtained upon structure optimization to ensure that the obtained ground state structures were at a minimum in the potential energy surface and thus dynamically stable. All computations were performed using a pruned grid (99 radial shells, 590 angular points per shell) along with a threshold of $< 10^{-10}$ for the root-mean-squared change in the density matrix during the self-consistent field procedure.

Time-dependent density functional theory (TD-DFT)[58, 59] single-point energy computations were performed at the same level of theory to identify the first 100 singlet excitations in both monomer and heterostructure systems. The first 100 singlet excitations of the optimized ground state heterostructures were also modeled with the HSE06 density functional[60] for comparison purposes while holding all other parameters constant. These simulations were further used to identify the optical energy gap (E_{opt}, defined as the energy of the first optically active excitation, where optical activity was determined by having an oscillator strength of at least 0.01) and the maximum absorption wavelength (λ_{max}). Simulated absorption spectra were generated using a full width at a half-max value of 0.1 eV. Additionally, the interlayer, intralayer, or hybrid (excitons comprising of both interlayer and intralayer character) nature of these excitations was identified using the intra-fragment charge transfer analysis (IFCT)[61] with the aid of Multiwfn 3.8.[62] Electron-hole pair generation for these systems primarily occurs from singlet excitations, as the TD-DFT calculations for triplet excitations depicted the forbidden nature of these transitions and thus will not be considered for further evaluation.

All electronic structure computations were performed using the Gaussian 16 software suite.[63] Counterpoise corrections[64] in Gaussian 16 were utilized to compute the counterpoise-corrected complexation energies to gauge the extent of basis set superposition error (BSSE) and its role in comparing the thermodynamic stability of the heterostructure systems. Additionally, Multiwfn 3.8 was employed to obtain cube files for the electron density differences (charge density difference or CDD) that occur during the formation of the heterostructure systems and the corresponding data for the local integration curves of electron density. Kohn-Sham orbital figures of the highest occupied molecular orbital (HOMO) and lowest unoccupied molecular orbital (LUMO) were constructed via projection onto the total electron density isosurface at 0.02 au. In comparison, electron accumulation and depletion regions corresponding to CDD analysis were plotted by projecting onto the total electron density isosurface at 0.0005 au.

3. RESULTS & DISCUSSION

Monomer Systems: The role of heteroatom doping in GQDs, particularly in the context of N, B, S, and Si doping,[65-67] has been widely studied and shown to alter the HOMO and LUMO orbitals. This often results in reduced fundamental gaps (defined as the HOMO-LUMO energy gap and sometimes used as an approximation to band gaps in periodic systems) and different absorption, emission, and excitonic properties compared to pristine GQDs. The dopants used in the current study effectively reduce the fundamental gap due to their varying orbital contributions to both HOMO and LUMO levels of the GQD, as depicted in Figure 1a. Group IV dopants primarily contribute to the LUMO level, reducing the LUMO energy and, thereby, the fundamental gap. In contrast, group VI dopants primarily affect the HOMO level, increasing its energy and reducing fundamental gaps. The geometric properties of the pristine quantum dot are locally perturbed due to the heteroatom dopants (Table S1), indicating a shift in hybridization away from sp^2 toward sp^3. This shift is more prominent for dopants with a considerably larger atomic radius than C, as

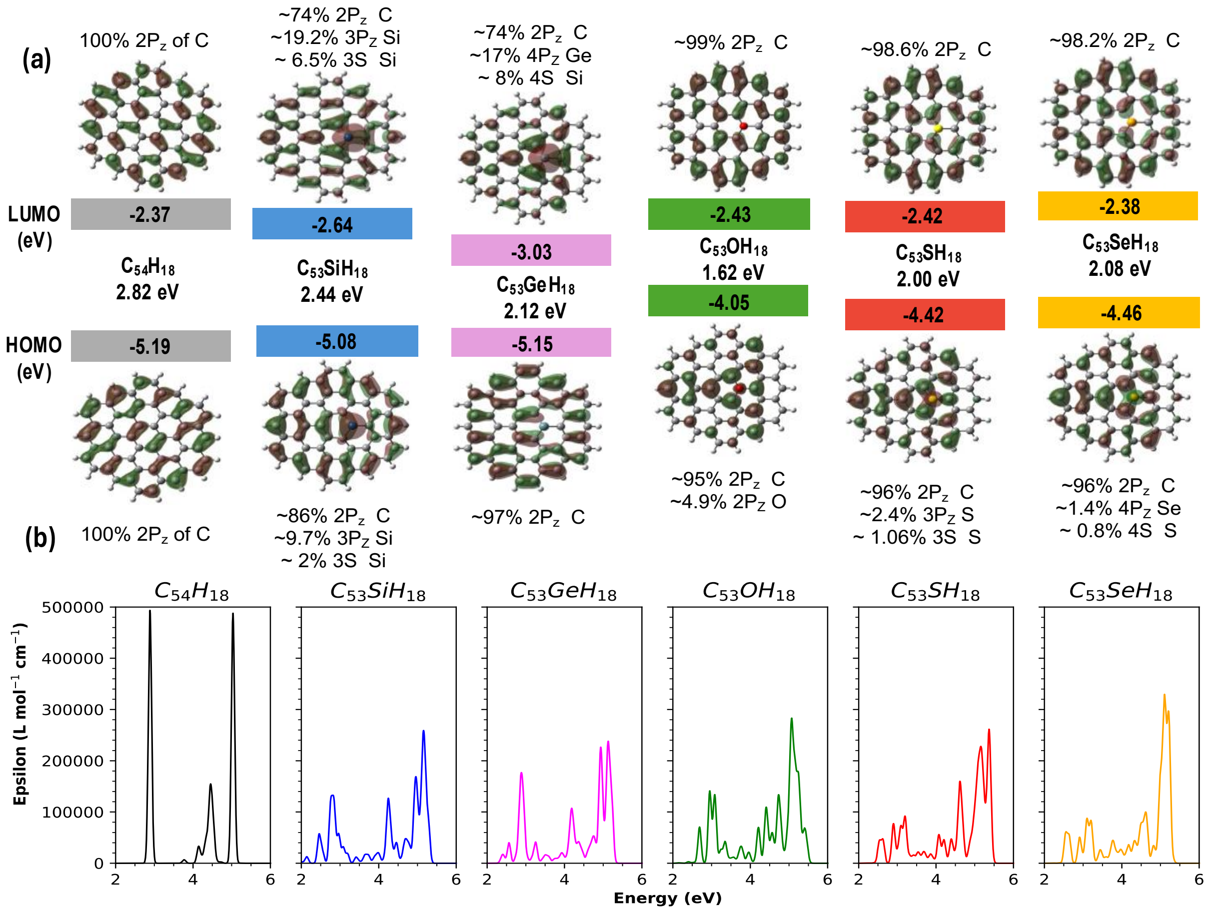

Figure 1. Optoelectronic properties of heteroatom-doped GQDs. (a) HOMO, LUMO levels and fundamental gaps with orbital contributions, (b) Optical absorption spectrum of GQDs.

evidenced by the increasing C-X bond lengths (1.42 – 1.90 Å) and reducing bond angles (119.9 – 95.7°) in Table S1. This change can be observed visually from a side-on view where the dopant atoms protrude out of the plane of the GQD. These dopant atoms have great potential as active sites owing to the electron density redistributions, as seen by the AIM (Atoms-in-molecules) charge distribution on these locations and the neighboring atoms (Figure S1). This analysis also revealed that the C atoms in neighboring sites to the heteroatom possess partial positive charges, except when O is used as a dopant due to the electronegativity differences. Thus, these heteroatom substitutions can reduce energy gaps while concurrently possessing characteristics of an active site to drive chemical transformations, which may be advantageous when constructing a final composite assembly. The effects to the GQD optical properties are depicted in Figure 1b. The nonmetal heteroatoms provide new excitation channels, as can be seen in the more continuous

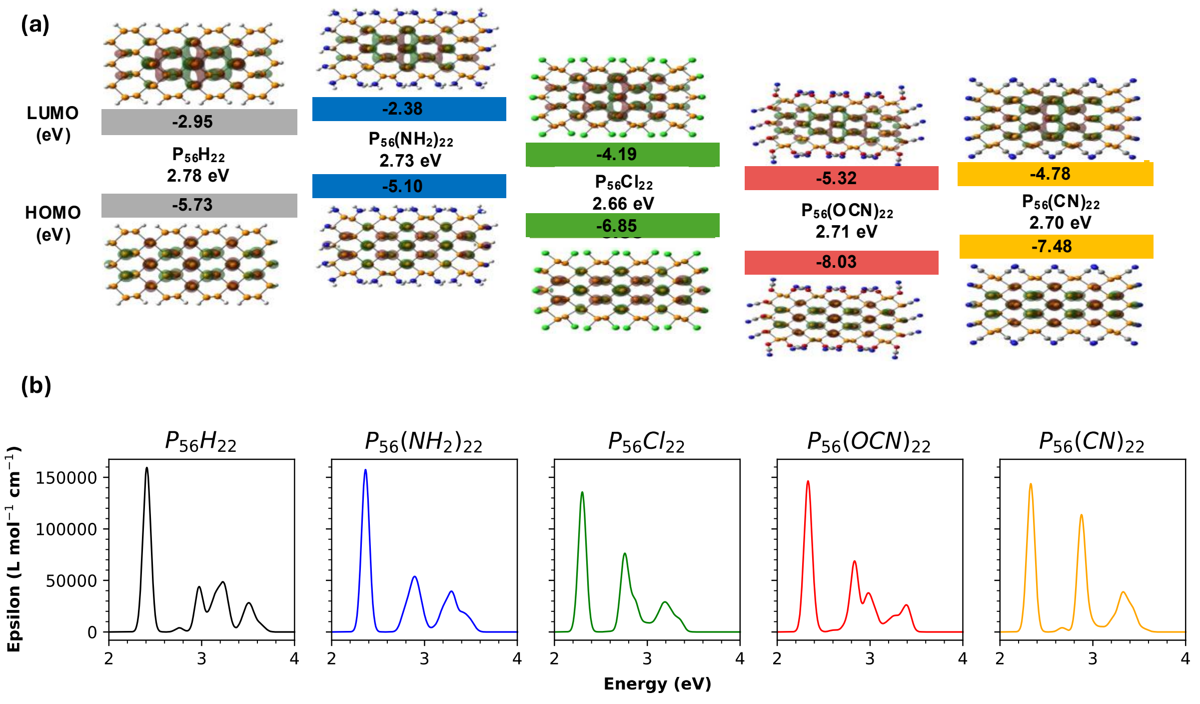

Figure 2. Optoelectronic properties of edge-functionalized PQDs. (a) HOMO, LUMO levels and fundamental gaps, (b) Optical absorption spectrum of PQDs.

spectra of the doped systems. However, this comes at the cost of reduced optical absorption intensities. This trend has also been observed in other theoretical investigations with different dopant atoms.[68]

The geometric properties (in-plane and out-of-plane bond lengths and angles between phosphorous atoms) of the edge-functionalized PQDs align with reports of pristine phosphorene and are discussed in our previous work.[54] The edge functional groups in these PQDs, unlike the heteroatom doping in GQD, do not compositionally contribute to the frontier molecular orbitals (FMOs; i.e. HOMO and LUMO), which are primarily comprised of 3*p* orbitals of phosphorous atoms as observed in Figure 2a. However, functionalization enables the repositioning of both HOMO and LUMO levels in a concerted fashion due to the edge dipole layers that are established from bond polarity at the periphery. This creates an electric field that shifts all particle energy levels similarly, which has been discussed in detail for PQD systems and 1D phosphorene nanowires.[29, 30, 54] As a result of the lack of compositional contribution from the edge states to the FMOs, which are involved in the excitations (refer to Figure 2b), the fundamental gaps, optical gaps, and the low energy portion of the absorption spectra for these systems remain essentially the same.

Heterostructure systems: Next, we delve into the formation of heterostructure systems using the previously discussed monomer QDs. Based on previous reports of optimized 2D vdW assemblies of phosphorene and graphene,[41] the optimized QD monomer systems used for this study were placed roughly 3.5 Å apart vertically (along the Z direction) and optimized to obtain the structure of the final heterostructure. A summary of the HOMO and LUMO energetics, predicted FMO alignments, and fundamental gaps for all 30 heterostructure systems can be found in the SI (Figure S2-S3 and Table S2). Since this work aims to create heterostructures capable of utilizing solar light to achieve higher power conversion efficiencies with effective charge carrier separation, we utilize screening criteria based on the monomer unit's FMO energy alignments. Here, we select systems that possess staggered HOMO and LUMO energetics (referred to as type II alignment and depicted in Figure S4) and ensure the HOMO and LUMO orbitals of the optimized heterostructures are localized in the separate layers, as this spatial separation is essential in reducing the exciton binding energy and charge carrier recombination. Additionally, we require these systems to possess a positive open circuit voltage (V_{OC}) value to facilitate power conversion (see values in Tables 1 and S2). Here V_{OC} is defined as

$$V_{OC} = E_{fund}^{Donor} - \Delta E_{LUMO} - 0.3 \tag{1}$$

where 0.3 eV is an approximate value used for losses associated with conversion kinetics.[69, 70] E_{fund}^{Donor} is the fundamental gap of the donor monomer, and ΔE_{LUMO} refers to the LUMO offset between the donor and acceptor units. Based on this screening, we reduced the candidate space to the ten systems discussed in the rest of this section. The interlayer separation (vdW gap) of these selected candidates, defined as the vertical distance between the top layer of the phosphorene basal plane and the graphene basal plane, ranges approximately from 3.12-3.43 Å (Table 1) indicating

Table 1 Summary of electronic properties of optimized heterostructures.

System	Predicted E_{fund} (eV)	Actual E_{fund} (eV)	ΔE_{fund} (eV)	V_{OC}	D-A e transfer	~ vdW gap (Å)
$C_{54}H_{18}$-$P_{56}H_{22}$	2.24	2.49	0.25	1.94	0.056	3.30
$C_{54}H_{18}$-$P_{56}Cl_{22}$	1.00	1.90	0.90	0.70	0.100	3.32
$C_{54}H_{18}$-$P_{56}CN_{22}$	0.41	1.74	1.33	0.11	0.151	3.33
$C_{53}SiH_{18}$-$P_{56}H_{22}$	2.13	2.38	0.25	1.83	0.063	3.20
$C_{53}SiH_{18}$-$P_{56}Cl_{22}$	0.89	1.82	0.92	0.59	0.091	3.37
$C_{53}GeH_{18}$-$P_{56}Cl_{22}$	0.96	1.84	0.88	0.66	0.089	3.38
$C_{53}GeH_{18}$-$P_{56}CN_{22}$	0.38	1.64	1.27	0.08	0.127	3.43
$C_{53}OH_{18}$-$P_{56}H_{22}$	1.10	1.42	0.32	0.80	0.075	3.28
$C_{53}SH_{18}$-$P_{56}H_{22}$	1.48	1.77	0.30	1.18	0.079	3.23
$C_{53}SeH_{18}$-$P_{56}H_{22}$	1.51	1.83	0.32	1.21	0.076	3.12

vdW interactions, and the interlayer separations are consistent with other low dimensional heterostructure candidates.[71]

To examine the thermodynamic stability of the heterostructures, the following quantities are defined:

$$\Delta G = \left[G_{het} - \left(G_{donor} + G_{acceptor}\right)\right]/n \tag{2}$$

$$\Delta E_{int} = \left[E_{het}^{het} - (E_{donor}^{het} - E_{acceptor}^{het})\right]/n \tag{3}$$

$$c.c. = (n\Delta E_{int} - BSSE)/n \tag{4}$$

$$\Delta E_{bind} = \left[E_{het}^{het} - (E_{donor}^{donor} - E_{acceptor}^{acceptor})\right]/n\ . \tag{5}$$

Here G_{het}, G_{donor}, and $G_{acceptor}$ are the sum of electronic and thermal free energy of the corresponding units, and ΔG is defined as the free energy of binding. In general, E refers to the total electronic energy of the units, while the superscript denotes the geometry at which the electronic energy was obtained. ΔE_{int} is defined as the interaction energy and is slightly different than the binding energy ΔE_{bind}, which accounts for the monomer deformation during heterostructure formation. The counterpoise corrected complexation energy ($c.c.$) is the difference between the interaction energy and BSSE. In all cases, n refers to the total number of atoms in each heterostructure system and has been utilized to represent these values on a per-atom basis to assess relative stability across the systems. Figure 3 depicts the energetic parameters demonstrating the interaction strength and thermodynamic stability. These energetic parameters indicate that heterostructure formation between phosphorene and graphene QDs is thermodynamically feasible. The counterpoise corrected complexation energies reveal that ΔE_{int} is sufficient for comparing relative interaction strengths amongst these candidates, as the trends are preserved even after accounting for the BSSE. However, they suggest that, on average, ΔE_{int} overestimates these interactions by roughly 0.16 – 0.23 kcal mol^{-1} per atom, with chloride functionalized systems

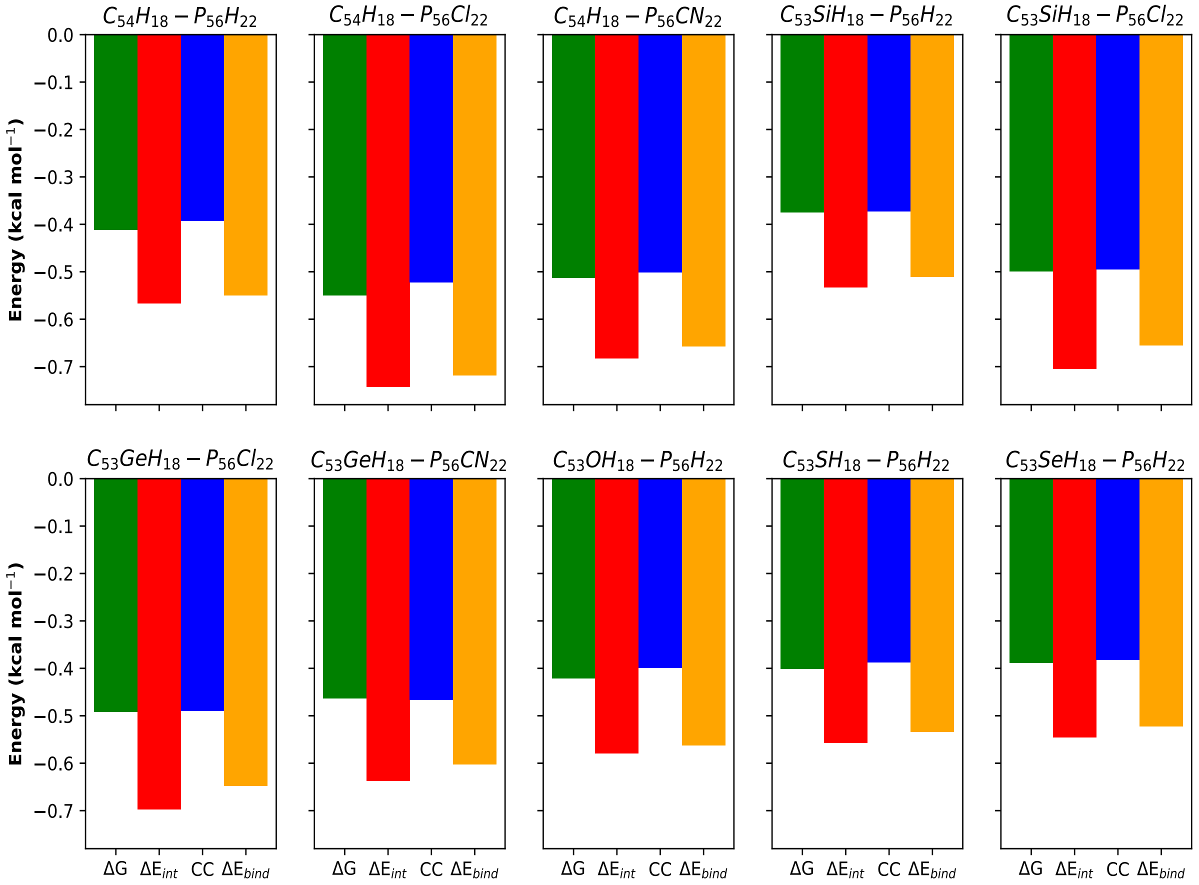

Figure 3. Thermodynamic stability of the selected donor-acceptor heterostructure systems.

having the highest over-estimation. The distinction between ΔE_{int} and ΔE_{bind} remains small, indicating that the monomer deformation during the formation of these composite heterostructures is minimal. However, the variation of this parameter amongst the considered heterostructures (see Table S3) reveals that systems with acceptor units having electron-withdrawing edge groups (Cl, CN, and OCN) have a relatively higher deformation. Figure S5 also unveils the tunability of interaction strength with the monomer modification technique. The acceptor PQD's edge terminating group has a larger impact on the interaction strengths than the GQD's dopant atom, likely due to the higher concentration of these modifications. Generally, the more electron-withdrawing edge groups (Cl, CN, OCN) on phosphorene will result in a higher electron transfer from the graphene unit to phosphorene due to its ability to pull electron density, which is indicated

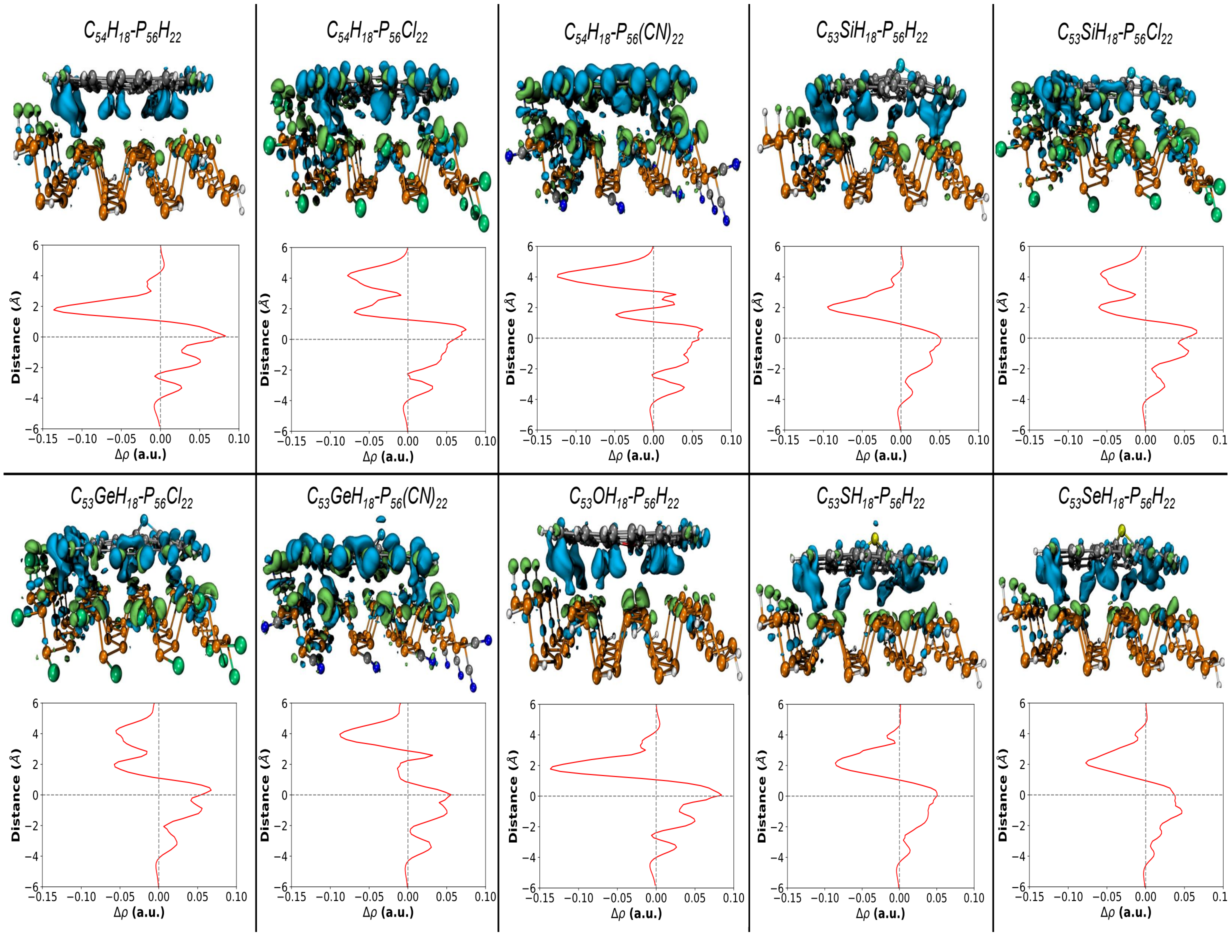

Figure 4. Charge density difference plots and local integral curves of electron density differences of selected donor-acceptor heterostructure systems. Blue isosurfaces indicate charge depletion, and lime green isosurfaces indicate charge accumulation.

by the NBO-determined charge transfer values in Table 1 (and Figure S6). These systems also possess more favorable interactions, as depicted in Figure S5. The higher charge transfer, better interaction energies, and larger monomer deformation indicate a higher degree of interlayer coupling in such systems. Thus, systems like $C_{54}H_{18}$-$P_{56}Cl_{22}$ or $C_{54}H_{18}$-$P_{56}CN_{22}$ possess a higher degree of interlayer coupling than their corresponding counterpart, $C_{54}H_{18}$-$P_{56}H_{22}$.

To further assess this and get a better idea of charge transfer during the formation of the heterostructures, we have plotted the charge density differentials (CDD) in Figure 4, which are obtained by plotting the difference in electron density of the heterostructure and the corresponding monomers in the heterostructure geometry. Typically, when two materials are brought together, a charge will be injected from the donor material to the acceptor material. Both NBO charge transfer and CDD analysis confirm electron injection from the GQD systems to PQD systems, aligning with our initial assumption of using the GQDs as donor candidates and PQDs as the acceptor candidates. It is worth noting that the local integral curves in Figure 4 denote the integration of the electron density differences in the xy plane (horizontal) for a given z value (vertical axis) that arises during heterostructure formation. The distance defined in the y-axis of these curves corresponds with the z-axis of the cartesian coordinate system for the heterostructures. Here, the xy plane cutting the $z = 0$ point aligns with the top layer of phosphorene atoms. The CDD isosurfaces and corresponding local integral curves in Figure 4 reveal that most of this charge rearrangement is concentrated at the interface regions. However, the charge injected into the phosphorene layer seems to propagate to the bottom layer of phosphorene atoms. The charge depleted from graphene for systems with Cl and CN functionalization also propagates above the interface region. Thus, the existence of type II-like donor-acceptor heterostructures coupled with charge transfer from donor GQDs to acceptor PQDs, which results in a built-in potential difference across the interface region (observed by $\Delta\rho$ of the local integral curves corresponding to the interface region), will drive electron-hole separation in these power conversion devices. It is worth mentioning that systems that are deemed to have a relatively higher degree of interlayer interactions through stability analysis and NBO charge transfer analysis (systems with Cl and CN functionalizations) display muted interlayer potential differences owing to the ease of charge propagation beyond the interfacial region, which is consistent with having stronger interlayer interactions.

Next, we shift the focus back to the electronic properties of the resulting heterostructure systems. As discussed previously, our primary focus is on systems that achieve a type II-like energetic alignment. This is depicted in Figure 5, along with the resulting optimized heterostructures HOMO and LUMO energetics. Here, we see a difference in these optimized heterostructure's predicted fundamental gap (derived from the HOMO and LUMO energetics of the individually optimized monomers) and actual fundamental gaps (derived from the HOMO and LUMO energies obtained post-optimization of the heterostructure systems). This difference is given by ΔE_{fund} in Table 1 and can be ascribed to the interlayer interaction, as systems deemed to

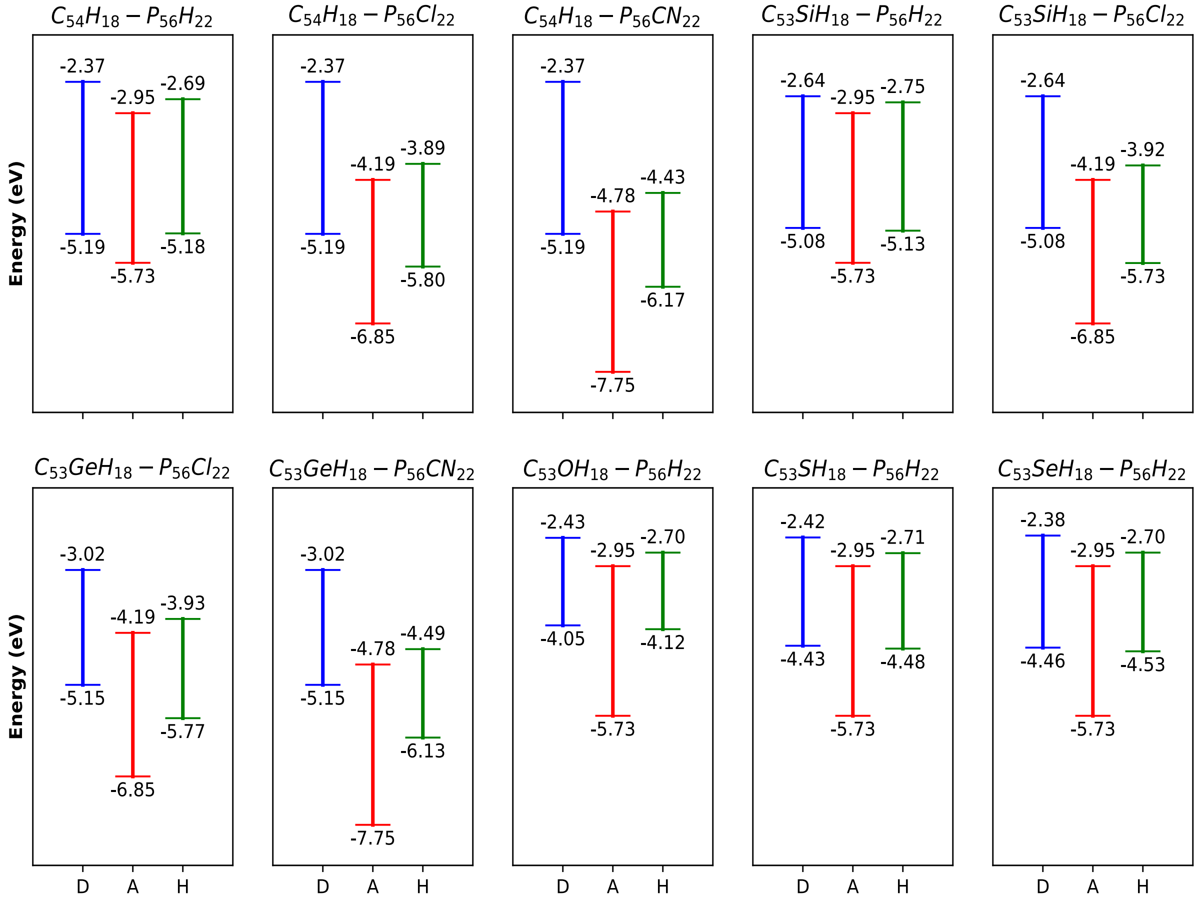

Figure 5. HOMO, LUMO orbital energies of selected donor-acceptor heterostructure systems with staggered alignments. D refers to the donor GQD, A refers to the acceptor PQD, and H refers to the resulting optimized heterostructure.

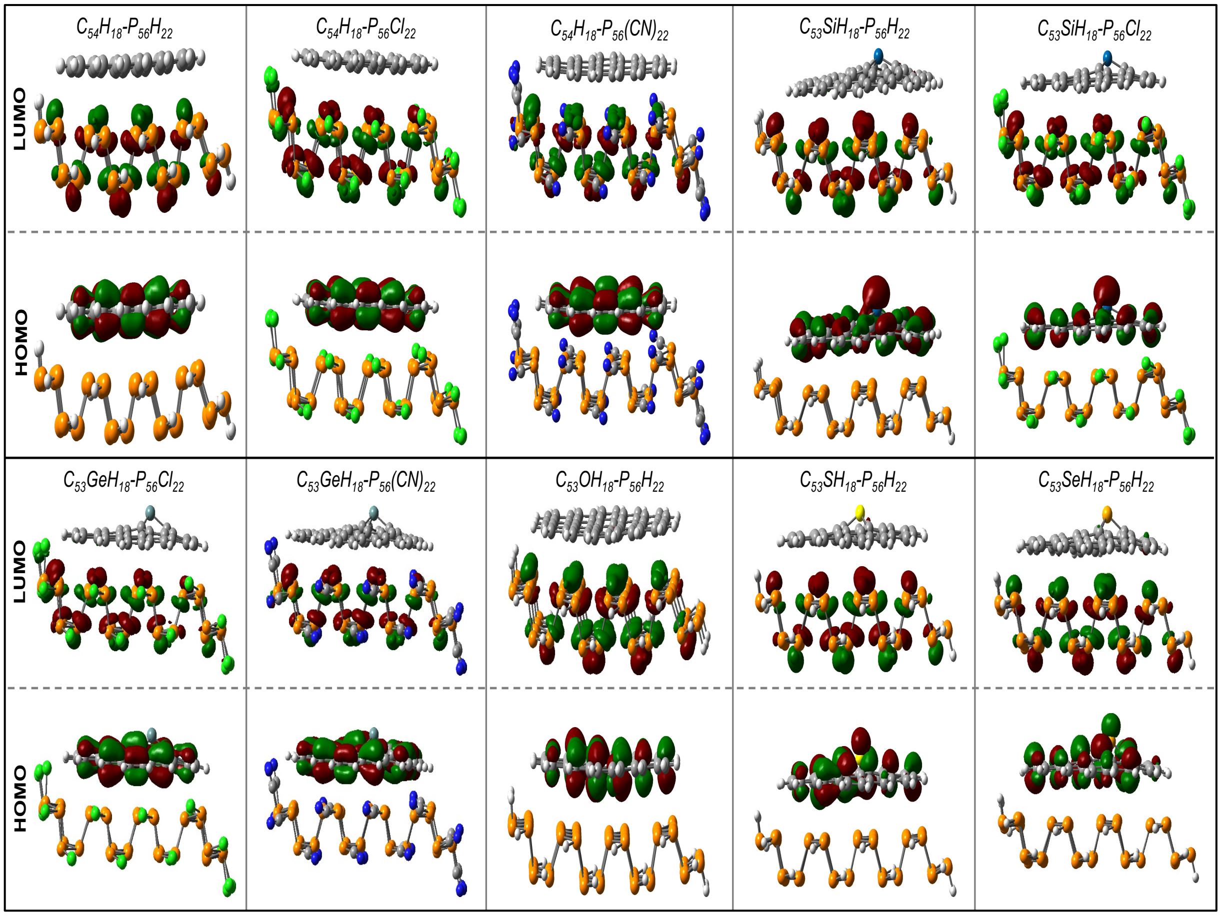

Figure 6. HOMO, LUMO orbital isosurfaces of the selected donor-acceptor heterostructure systems with staggered energy alignments.

have a higher degree of interlayer interaction (and deformation) from the previous sections have higher ΔE_{fund} values. Figure 6 depicts the isosurfaces of the spatially separated HOMO and LUMO orbitals of the ten heterostructure candidates. These orbitals remain largely undisturbed and compositionally akin to the individual monomer counterparts, indicating that despite the varying levels of interlayer interactions, none of the ten candidates possess strong enough interactions to promote compositional changes to the FMOs inducing charge delocalization. This is important in maintaining charge carrier separation, as stronger interlayer interactions can result in delocalized FMO states, which can reduce charge carrier separation. Additionally, we see a reduction in fundamental gaps of all the heterostructure systems compared to the individual monomer counterparts (Table 1), enabling these systems to have fundamental gaps better suited for optimizing visible light absorption.

Subsequently, we focus on the optical absorption of the resulting heterostructure systems. Figure 7 depicts the simulated absorption spectra from the first 100 singlet excitations, denoted by the UV-Vis response curves. The color-coded traces correspond to the contributions to the total response curve arising from a local perturbation in the donor (D curve) or acceptor (A curve) environment or a charge transfer excitation (D→A or A→D curves) between these monomer units. The maximum solar spectral irradiance roughly corresponds to the visible light region. Thus, a

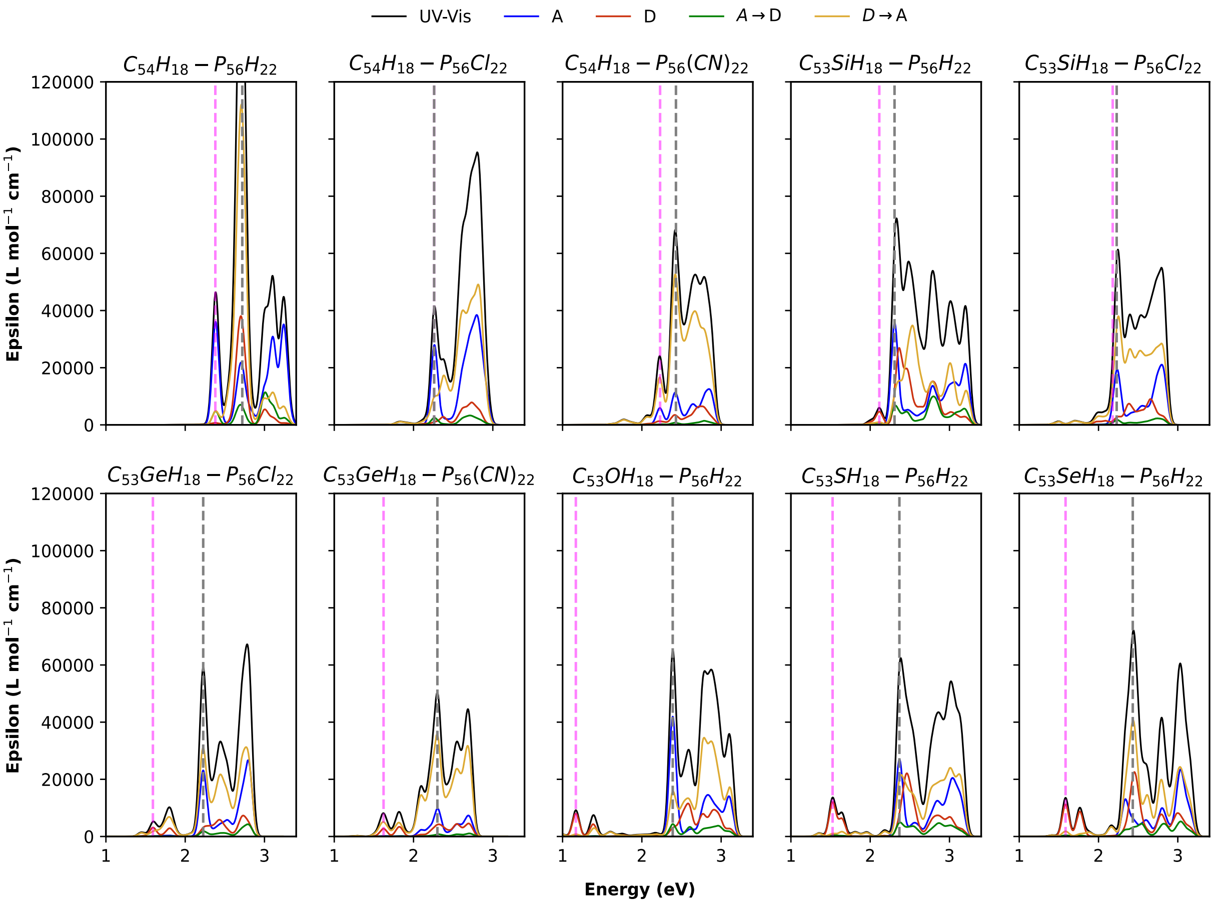

Figure 7. Simulated absorption spectra of selected donor-acceptor heterostructure systems. Total response of the heterostructure is depicted by the UV-Vis curve, while colored traces indicate the local response associated with the acceptor (A), donor (D), or charge transfer (A→D or D→A). Dashed vertical lines correspond to λ_{max} (grey) and the E_{opt} excitation (magenta).

power conversion device utilizing solar light should ideally have continuous and intense absorptions around ~ 1.5 eV – 3.3 eV (380 nm – 700 nm) to maximize solar energy absorption. The heterostructure systems have new excitation channels within this desired range compared to their monomer counterparts (Figure 1b and Figure 2b) owing to the additional charge transfer excitations denoted by the green and yellow curves in Figure 7. Additionally, heteroatom doping, which reduced the optical gap of the donor, has enabled the corresponding heterostructures to have excitations around the low energy region of the desired range (~ 1.5 eV), thereby increasing the absorbance range. The optical absorption spectrum of these heterostructures is a combination of the individual donor and acceptor spectra with additional charge transfer excitations. As a result, more excitations are present, but there is a considerable decrease in the absorption intensity. This can be observed by the muted features of the red and blue response curves (in Figure 7) that arise roughly around the same excitation energies as those in Figure 1a and Figure 1b. This can be ascribed to the long-range nature of charge transfer excitations, which are the prominent contributors to the total response curves in Figure 7. The reduction in intensity in these long-ranged excitations typically stems from the lower overlap between initial and final states, reducing transition dipole moments and, thereby, the absorption intensities. The λ_{max} feature for all heterostructure systems (denoted by the vertical grey dotted line in Figure 7) typically corresponds to a point where all or most types of inter-fragment and intra-fragment excitations can coincide. In contrast, the E_{opt} excitation (denoted by the vertical magenta lines in Figure 7) mainly corresponds to the lower E_{opt} excitations of the two contributing monomers, with some occasional charge transfer contributions. Thus, E_{opt} in the heterostructure systems primarily arise due to intralayer transitions in the donor, except for systems with undoped GQDs where intralayer transitions in the acceptor become the primary contributor. It is worth mentioning that there are dark excitations (f

~ 0), which are primarily HOMO-LUMO transitions (~99% contribution) arising before the defined E_{opt} excitations in these heterostructure systems, which can be attributed to the lack of overlap between these orbitals. The total UV-Vis response has also been obtained with the HSE06 functional (see Figure S7), and the similarity depicted between the response curves is evident.

Finally, we quantify the power conversion efficiency (PCE) of these heterostructure systems based on Scharber's model, which approximates the fraction of incident power converted to electricity[72] by using the following functional form to estimate the power output over the input power. This model has been widely employed in similar theoretical work for other low-dimensional materials.[30, 73]

$$PCE = \frac{\beta_{FF} V_{OC} J_{sc}}{P_{solar}} \tag{6}$$

The power output of a device is dependent on the fill factor ($\beta_{FF} = 0.65$), the open circuit voltage (V_{OC} which is the maximum voltage at zero current and is defined in Equation 1) and the short circuit current density (J_{sc} which is the maximum current flow at zero voltage). Here J_{sc} is defined as $J_{sc} = \int_{E_{fund}^{Donor}}^{\infty} \frac{p(\hbar\omega)d(\hbar\omega)}{\hbar\omega}$. It is noteworthy that the power out of these devices is largely dependent on electronic structure factors, like the fundamental gap of donor units (captured within the short circuit current density calculation) and the energy difference in the donor's HOMO and acceptor's LUMO (captured within the open circuit voltage). The input power is defined as $P_{solar} = \int_0^{\infty} p(\hbar\omega)d(\hbar\omega) = 1000\,W/m^2$, where $p(\hbar\omega)$ is the AM1.5 solar energy flux at the photon energy $\hbar\omega$. It is important to note that the model assumes an external quantum efficiency of 100%. Although slightly red-shifted, the optical gaps in the optimized heterostructure systems closely resemble the donor monomer's fundamental gap. Thus, using the corresponding donor fundamental gap as the lower integration limit in the short circuit current density calculation is a conservative approximation that can capture the trends observed between the optimized heterostructure systems. However, it is worth noting that the expression for V_{OC} (Eq. 1), which utilizes the individual monomer energetics, may fail to accurately reproduce the trends observed in all the optimized heterostructures due to the changes in the electronic structure of heterostructures, particularly with higher interlayer interactions. Considering that there is a slight decrease in the charge separation ability of these strongly interacting systems (Cl and CN functionalized systems), we can utilize the PCE values for heterostructures with hydrogen edge functionalizations in their acceptor units (those deemed to be better performing in terms of charge carrier segregation and where the electronic structure changes are minimal, i.e. $\Delta E_{\text{fund}} <$ 0.35 eV) to best distinguish between device performance. In doing so, we identify that these hydrogen-functionalized systems possess PCE% values between 11 – 29% (Table 2), where the higher PCE% values can largely be attributed to the dopant-led band gap lowering of the donor units, as witnessed by the enhancement in J_{sc} of these systems.

Table 2. Power conversion performance of heterostructure systems.

System	V_{OC} (eV)	J_{sc} (W/m^{2}eV)	PCE%
$C_{54}H_{18}$-$P_{56}H_{22}$	1.94	92.86	11.71
$C_{54}H_{18}$-$P_{56}Cl_{22}$	0.70	92.86	4.22
$C_{54}H_{18}$-$P_{56}CN_{22}$	0.11	92.86	0.66
$C_{53}SiH_{18}$-$P_{56}H_{22}$	1.83	198.73	23.64
$C_{53}SiH_{18}$-$P_{56}Cl_{22}$	0.59	198.73	7.62
$C_{53}GeH_{18}$-$P_{56}Cl_{22}$	0.66	314.13	13.48
$C_{53}GeH_{18}$-$P_{56}CN_{22}$	0.08	314.13	1.63
$C_{53}OH_{18}$-$P_{56}H_{22}$	0.80	549.66	28.58
$C_{53}SH_{18}$-$P_{56}H_{22}$	1.18	365.25	28.01
$C_{53}SeH_{18}$-$P_{56}H_{22}$	1.21	331.55	26.08

4. CONCLUSIONS

In summary, we employ DFT and TD-DFT computations to illustrate the optoelectronic properties of van der Waals heterostructure quantum dots capable of solar energy conversion, formed using hydrogen-terminated doped GQDs and edge-functionalized PQDs. We systematically evaluate the synergistic effects of doping GQDs with novel heteroatoms like Si, Ge, O, S, and Se and edge functionalizing PQDs with groups like H, NH_2, Cl, OCN, and CN. These modification techniques work by either compositionally affecting the HOMO and LUMO orbitals of donor molecules or by shifting the orbital energies of the acceptor molecules. This approach results in 10 out of 30 heterostructure candidates attaining staggered energy alignment (type-II) with spatial separation of HOMO and LUMO orbitals along with a positive open circuit voltage. Additionally, these modulations produce varying degrees of interlayer coupling, which plays a role in the resulting electronic properties and charge carrier separation. Out of the ten candidates discussed in this work, the heterostructures with lower interlayer coupling were deemed better for charge carrier separation, owing to the higher potential difference at the interface and the ability to oppose charge carrier recombination. These systems also have better open circuit voltages, short circuit current densities, and, as a result, higher power conversion efficiencies, rendering them ideal candidates for power conversion applications like photovoltaics or photocatalysis.

5. SUPPORTING INFORMATION

The Supporting Information is available free of charge on the ACS Publications website at DOI: xxx.xxx.

Geometric properties around dopant site in graphene quantum dots; AIM charges around the dopant site of $C_{53}XH_{18}$; HOMO, LUMO orbital energies of undoped and Si, Ge-doped heterostructure systems; HOMO, LUMO orbital energies of O, S, and Se-doped heterostructure systems; Electronic properties of all heterostructure systems; Depiction of Type I, Type II, and Type III band alignment; Thermodynamic stability of all donor-acceptor heterostructure systems;

Binding and interaction energies of all heterostructure candidates; Donor-acceptor electron transfer from GQD to PQD; Simulated absorption spectra using B3LYP+GD3 and HSE06.

6. ACKNOWLEDGEMENTS

The material was based upon work supported by the National Science Foundation under Grant No. 2147956. The authors acknowledge Baylor High Performance and Research Computing Services for supporting the research reported in this paper.

7. REFERENCES

(1) Ang, T.-Z.; Salem, M.; Kamarol, M.; Das, H. S.; Nazari, M. A.; Prabaharan, N. A comprehensive study of renewable energy sources: Classifications, challenges and suggestions. *Energy Strategy Reviews* **2022**, *43*, 100939. DOI: https://doi.org/10.1016/j.esr.2022.100939.

(2) Khan, K.; Tareen, A. K.; Aslam, M.; Wang, R.; Zhang, Y.; Mahmood, A.; Ouyang, Z.; Zhang, H.; Guo, Z. Recent developments in emerging two-dimensional materials and their applications. *Journal of Materials Chemistry C* **2020**, *8* (2), 387-440, 10.1039/C9TC04187G. DOI: 10.1039/C9TC04187G.

(3) Yagmurcukardes, M.; Peeters, F. M.; Senger, R. T.; Sahin, H. Nanoribbons: From fundamentals to state-of-the-art applications. *Applied Physics Reviews* **2016**, *3*, 041302. DOI: 10.1063/1.4966963.

(4) Bera, D.; Qian, L.; Tseng, T.-K.; Holloway, P. H. Quantum Dots and Their Multimodal Applications: A Review. *Materials* **2010**, *3* (4), 2260-2345.

(5) Novoselov, K. S.; Geim, A. K.; Morozov, S. V.; Jiang, D.; Zhang, Y.; Dubonos, S. V.; Grigorieva, I. V.; Firsov, A. A. Electric Field Effect in Atomically Thin Carbon Films. *Science* **2004**, *306* (5696), 666-669. DOI: 10.1126/science.1102896 .

(6) Novoselov, K. S.; Jiang, D.; Schedin, F.; Booth, T. J.; Khotkevich, V. V.; Morozov, S. V.; Geim, A. K. Two-dimensional atomic crystals. *Proceedings of the National Academy of Sciences of the United States of America* **2005**, *102* (30), 10451. DOI: 10.1073/pnas.0502848102.

(7) Castellanos-Gomez, A.; Vicarelli, L.; Prada, E.; Island, J. O.; Narasimha-Acharya, K. L.; Blanter, S. I.; Groenendijk, D. J.; Buscema, M.; Steele, G. A.; Alvarez, J. V.; et al. Isolation and characterization of few-layer black phosphorus. *2D Materials* **2014**, *1* (2), 025001. DOI: 10.1088/2053-1583/1/2/025001.

(8) Splendiani, A.; Sun, L.; Zhang, Y.; Li, T.; Kim, J.; Chim, C. Y.; Galli, G.; Wang, F. Emerging photoluminescence in monolayer MoS2. *Nano Lett* **2010**, *10* (4), 1271-1275. DOI: 10.1021/nl903868w From NLM.

(9) Thomas, A.; Fischer, A.; Goettmann, F.; Antonietti, M.; Müller, J.-O.; Schlögl, R.; Carlsson, J. M. Graphitic carbon nitride materials: variation of structure and morphology and their use as metal-free catalysts. *Journal of Materials Chemistry* **2008**, *18* (41), 4893-4908, 10.1039/B800274F. DOI: 10.1039/B800274F.

(10) Kubota, Y.; Watanabe, K.; Tsuda, O.; Taniguchi, T. Deep Ultraviolet Light-Emitting Hexagonal Boron Nitride Synthesized at Atmospheric Pressure. *Science* **2007**, *317* (5840), 932-934. DOI: doi:10.1126/science.1144216.

(11) Crystal Structure of Barium Titanate. *Nature* **1945**, *155* (3938), 484-485. DOI: 10.1038/155484b0.

(12) Naguib, M.; Kurtoglu, M.; Presser, V.; Lu, J.; Niu, J.; Heon, M.; Hultman, L.; Gogotsi, Y.; Barsoum, M. W. Two-Dimensional Nanocrystals Produced by Exfoliation of Ti3AlC2. *Advanced Materials* **2011**, *23* (37), 4248-4253. DOI: https://doi.org/10.1002/adma.201102306.

(13) Zeng, M.; Xiao, Y.; Liu, J.; Yang, K.; Fu, L. Exploring Two-Dimensional Materials toward the Next-Generation Circuits: From Monomer Design to Assembly Control. *Chemical Reviews* **2018**, *118* (13), 6236-6296. DOI: 10.1021/acs.chemrev.7b00633.

(14) Tung, R. T. Chemical Bonding and Fermi Level Pinning at Metal-Semiconductor Interfaces. *Physical Review Letters* **2000**, *84* (26), 6078-6081. DOI: 10.1103/PhysRevLett.84.6078.

(15) Matthews, J. W.; Blakeslee, A. E. Defects in epitaxial multilayers: I. Misfit dislocations. *Journal of Crystal Growth* **1974**, *27*, 118-125. DOI: https://doi.org/10.1016/S0022-0248(74)80055-2.

(16) Bhat, T. N.; Rajpalke, M. K.; Roul, B.; Kumar, M.; Krupanidhi, S. B. Substrate nitridation induced modulations in transport properties of wurtzite GaN/p-Si (100) heterojunctions grown by molecular beam epitaxy. *Journal of Applied Physics* **2011**, *110*, 093718. DOI: 10.1063/1.3658867.

(17) Faugier-Tovar, J.; Lazar, F.; Marichy, C.; Brylinski, C. Influence of the Lattice Mismatch on the Atomic Ordering of ZnO Grown by Atomic Layer Deposition onto Single Crystal Surfaces with Variable Mismatch (InP, GaAs, GaN, SiC). *Condensed Matter* **2017**, *2* (1), 3.

(18) Liang, S.-J.; Cheng, B.; Cui, X.; Miao, F. Van der Waals Heterostructures for High-Performance Device Applications: Challenges and Opportunities. *Advanced Materials* **2020**, *32* (27), 1903800. DOI: https://doi.org/10.1002/adma.201903800.

(19) Wang, P.; Jia, C.; Huang, Y.; Duan, X. Van der Waals Heterostructures by Design: From 1D and 2D to 3D. *Matter* **2021**, *4* (2), 552-581. DOI: https://doi.org/10.1016/j.matt.2020.12.015.

(20) Geim, A. K.; Grigorieva, I. V. Van der Waals heterostructures. *Nature* **2013**, *499* (7459), 419-425. DOI: 10.1038/nature12385.

(21) Barré, E.; Dandu, M.; Kundu, S.; Sood, A.; da Jornada, F. H.; Raja, A. Engineering interlayer hybridization in van der Waals bilayers. *Nature Reviews Materials* **2024**, 9, 499-508. DOI: 10.1038/s41578-024-00666-1.

(22) Pham, K. D.; Nguyen, C. V.; Binh, N. T. T.; Nguyen, C. Q.; Idrees, M.; Amin, B.; Nguyen, S.-T.; Hieu, N. V. Two-dimensional blue phosphorene–BAs vdW heterostructure with optical and photocatalytic properties: a first-principles study. *RSC Advances* **2021**, *11* (21), 13025-13029, 10.1039/D1RA00004G. DOI: 10.1039/D1RA00004G.

(23) Ashwin Kishore, M. R.; Larsson, K.; Ravindran, P. Two-Dimensional CdX/C2N (X = S, Se) Heterostructures as Potential Photocatalysts for Water Splitting: A DFT Study. *ACS Omega* **2020**, *5* (37), 23762-23768. DOI: 10.1021/acsomega.0c02804.

(24) Jia, X.; Wang, J.; Lu, Y.; Sun, J.; Li, Y.; Wang, Y.; Zhang, J. Designing SnS/MoS2 van der Waals heterojunction for direct Z-scheme photocatalytic overall water-splitting by DFT investigation. *Physical Chemistry Chemical Physics* **2022**, *24* (35), 21321-21330, 10.1039/D2CP02692A. DOI: 10.1039/D2CP02692A.

(25) Bernardi, M.; Palummo, M.; Grossman, J. C. Extraordinary Sunlight Absorption and One Nanometer Thick Photovoltaics Using Two-Dimensional Monolayer Materials. *Nano Letters* **2013**, *13* (8), 3664-3670. DOI: 10.1021/nl401544y.

(26) Ceballos, F.; Bellus, M. Z.; Chiu, H.-Y.; Zhao, H. Ultrafast Charge Separation and Indirect Exciton Formation in a MoS2–MoSe2 van der Waals Heterostructure. *ACS Nano* **2014**, *8* (12), 12717-12724. DOI: 10.1021/nn505736z.

(27) Wang, J.; Guan, Z.; Huang, J.; Li, Q.; Yang, J. Enhanced photocatalytic mechanism for the hybrid g-C3N4/MoS2 nanocomposite. *Journal of Materials Chemistry A* **2014**, *2* (21), 7960-7966, 10.1039/C4TA00275J. DOI: 10.1039/C4TA00275J.

(28) Dai, J.; Zeng, X. C. Bilayer Phosphorene: Effect of Stacking Order on Bandgap and Its Potential Applications in Thin-Film Solar Cells. *The Journal of Physical Chemistry Letters* **2014**, *5* (7), 1289-1293. DOI: 10.1021/jz500409m.

(29) Hu, W.; Lin, L.; Zhang, R.; Yang, C.; Yang, J. Highly Efficient Photocatalytic Water Splitting over Edge-Modified Phosphorene Nanoribbons. *Journal of the American Chemical Society* **2017**, *139* (43), 15429-15436. DOI: 10.1021/jacs.7b08474.

(30) Hu, W.; Lin, L.; Yang, C.; Dai, J.; Yang, J. Edge-Modified Phosphorene Nanoflake Heterojunctions as Highly Efficient Solar Cells. *Nano Letters* **2016**, *16* (3), 1675-1682. DOI: 10.1021/acs.nanolett.5b04593.

(31) Kar, M.; Sarkar, R.; Pal, S.; Sarkar, P. Edge-Modified Phosphorene Antidot Nanoflakes and Their van der Waals Heterojunctions for Solar Cell Applications. *The Journal of Physical Chemistry C* **2019**, *123* (34), 20748-20756. DOI: 10.1021/acs.jpcc.9b05307.

(32) Abdelsalam, H.; Atta, M. M.; Osman, W.; Zhang, Q. Two-dimensional quantum dots for highly efficient heterojunction solar cells. *Journal of Colloid and Interface Science* **2021**, *603*, 48-57. DOI: https://doi.org/10.1016/j.jcis.2021.06.121.

(33) Hagel, J.; Brem, S.; Malic, E. Electrical tuning of moiré excitons in MoSe2 bilayers. *2D Materials* **2023**, *10* (1), 014013. DOI: 10.1088/2053-1583/aca916.

(34) Leisgang, N.; Shree, S.; Paradisanos, I.; Sponfeldner, L.; Robert, C.; Lagarde, D.; Balocchi, A.; Watanabe, K.; Taniguchi, T.; Marie, X.; et al. Giant Stark splitting of an exciton in bilayer MoS2. *Nature Nanotechnology* **2020**, *15* (11), 901-907. DOI: 10.1038/s41565-020-0750-1.

(35) Choi, J.; Florian, M.; Steinhoff, A.; Erben, D.; Tran, K.; Kim, D. S.; Sun, L.; Quan, J.; Claassen, R.; Majumder, S.; et al. Twist Angle-Dependent Interlayer Exciton Lifetimes in van der Waals Heterostructures. *Physical Review Letters* **2021**, *126* (4), 047401. DOI: 10.1103/PhysRevLett.126.047401.

(36) Steeger, P.; Graalmann, J.-H.; Schmidt, R.; Kupenko, I.; Sanchez-Valle, C.; Marauhn, P.; Deilmann, T.; de Vasconcellos, S. M.; Rohlfing, M.; Bratschitsch, R. Pressure Dependence of Intra- and Interlayer Excitons in 2H-MoS2 Bilayers. *Nano Letters* **2023**, *23* (19), 8947-8952. DOI: 10.1021/acs.nanolett.3c02428.

(37) Montblanch, A. R. P.; Kara, D. M.; Paradisanos, I.; Purser, C. M.; Feuer, M. S. G.; Alexeev, E. M.; Stefan, L.; Qin, Y.; Blei, M.; Wang, G.; et al. Confinement of long-lived interlayer excitons in WS2/WSe2 heterostructures. *Communications Physics* **2021**, *4* (1), 119. DOI: 10.1038/s42005-021-00625-0.

(38) Padilha, J. E.; Fazzio, A.; da Silva, A. J. R. van der Waals Heterostructure of Phosphorene and Graphene: Tuning the Schottky Barrier and Doping by Electrostatic Gating. *Physical Review Letters* **2015**, *114* (6), 066803. DOI: 10.1103/PhysRevLett.114.066803.

(39) Hu, W.; Wang, T.; Yang, J. Tunable Schottky contacts in hybrid graphene–phosphorene nanocomposites. *Journal of Materials Chemistry C* **2015**, *3* (18), 4756-4761, 10.1039/C5TC00759C. DOI: 10.1039/C5TC00759C.

(40) Rebolledo Espinoza, C.; Ryndyk, D. A.; Dianat, A.; Gutierrez, R.; Cuniberti, G. First principles study of field effect device through van der Waals and lateral heterostructures of graphene, phosphorene and graphane. *Nano Materials Science* **2022**, *4* (1), 52-59. DOI: https://doi.org/10.1016/j.nanoms.2020.12.005.

(41) Cai, Y.; Zhang, G.; Zhang, Y.-W. Electronic Properties of Phosphorene/Graphene and Phosphorene/Hexagonal Boron Nitride Heterostructures. *The Journal of Physical Chemistry C* **2015**, *119* (24), 13929-13936. DOI: 10.1021/acs.jpcc.5b02634.

(42) Pei, Q.-X.; Zhang, X.; Ding, Z.; Zhang, Y.-Y.; Zhang, Y.-W. Thermal stability and thermal conductivity of phosphorene in phosphorene/graphene van der Waals heterostructures. *Physical Chemistry Chemical Physics* **2017**, *19* (26), 17180-17186, 10.1039/C7CP02553J. DOI: 10.1039/C7CP02553J.

(43) Pei, J.; Gai, X.; Yang, J.; Wang, X.; Yu, Z.; Choi, D. Y.; Luther-Davies, B.; Lu, Y. Producing air-stable monolayers of phosphorene and their defect engineering. *Nat Commun* **2016**, *7*, 10450. DOI: 10.1038/ncomms10450 From NLM.

(44) Liu, H.; Neal, A. T.; Zhu, Z.; Luo, Z.; Xu, X.; Tománek, D.; Ye, P. D. Phosphorene: An Unexplored 2D Semiconductor with a High Hole Mobility. *ACS Nano* **2014**, *8* (4), 4033-4041. DOI: 10.1021/nn501226z.

(45) De Alwis, W. M. U. G.; Shuford, K. L. Anisotropic Behavior of Optical Properties in Edge-Modified Phosphorene Quantum Dots. *The Journal of Physical Chemistry C* **2023**, *127* (23), 11085-11093. DOI: 10.1021/acs.jpcc.3c01463.

(46) Jiang, J.-W.; Park, H. S. Mechanical properties of single-layer black phosphorus. *Journal of Physics D: Applied Physics* **2014**, *47* (38), 385304. DOI: 10.1088/0022-3727/47/38/385304.

(47) Jang, H.; Wood, J. D.; Ryder, C. R.; Hersam, M. C.; Cahill, D. G. Anisotropic Thermal Conductivity of Exfoliated Black Phosphorus. *Advanced Materials* **2015**, *27* (48), 8017-8022. DOI: https://doi.org/10.1002/adma.201503466.

(48) Gao, W.; Zhou, Y.; Wu, X.; Shen, Q.; Ye, J.; Zou, Z. State-of-the-Art Progress in Diverse Black Phosphorus-Based Structures: Basic Properties, Synthesis, Stability, Photo- and

Electrocatalysis-Driven Energy Conversion. *Advanced Functional Materials* **2021**, *31* (3), 2005197. DOI: https://doi.org/10.1002/adfm.202005197.

(49) Wang, G.; Slough, W. J.; Pandey, R.; Karna, S. P. Degradation of phosphorene in air: understanding at atomic level. *2D Materials* **2016**, *3* (2), 025011. DOI: 10.1088/2053-1583/3/2/025011.

(50) Zou, Y.; Hou, X.; Wei, H.; Shao, J.; Jiang, Q.; Ren, L.; Wu, J. Circumcoronenes. *Angewandte Chemie International Edition* **2023**, *62* (19), e202301041. DOI: https://doi.org/10.1002/anie.202301041.

(51) Feng, J.; Guo, Q.; Song, N.; Liu, H.; Dong, H.; Chen, Y.; Yu, L.; Dong, L. Density functional theory study on optical and electronic properties of co-doped graphene quantum dots based on different nitrogen doping patterns. *Diamond and Related Materials* **2021**, *113*, 108264. DOI: https://doi.org/10.1016/j.diamond.2021.108264.

(52) Fazio, G.; Ferrighi, L.; Di Valentin, C. Boron-doped graphene as active electrocatalyst for oxygen reduction reaction at a fuel-cell cathode. *Journal of Catalysis* **2014**, *318*, 203-210. DOI: https://doi.org/10.1016/j.jcat.2014.07.024.

(53) Favaro, M.; Ferrighi, L.; Fazio, G.; Colazzo, L.; Di Valentin, C.; Durante, C.; Sedona, F.; Gennaro, A.; Agnoli, S.; Granozzi, G. Single and Multiple Doping in Graphene Quantum Dots: Unraveling the Origin of Selectivity in the Oxygen Reduction Reaction. *ACS Catalysis* **2015**, *5* (1), 129-144. DOI: 10.1021/cs501211h.

(54) De Alwis, W. M. U. G.; Weerawardene, K. L. D. M.; Ellington, T. L.; Shuford, K. L. Electronic Structure Modification of Rectangular Phosphorene Quantum Dots Via Edge Passivation. *The Journal of Physical Chemistry C* **2021**, *125* (9), 5029-5036. DOI: 10.1021/acs.jpcc.0c09722.

(55) Becke, A. D. Density-functional thermochemistry. III. The role of exact exchange. *The Journal of Chemical Physics* **1993**, *98* (7), 5648-5652. DOI: 10.1063/1.464913.

(56) Stephens, P. J.; Devlin, F. J.; Chabalowski, C. F.; Frisch, M. J. Ab Initio Calculation of Vibrational Absorption and Circular Dichroism Spectra Using Density Functional Force Fields. *The Journal of Physical Chemistry* **1994**, *98* (45), 11623-11627. DOI: 10.1021/j100096a001.

(57) Grimme, S.; Antony, J.; Ehrlich, S.; Krieg, H. A consistent and accurate ab initio parametrization of density functional dispersion correction (DFT-D) for the 94 elements H-Pu. *The Journal of Chemical Physics* **2010**, *132*, 154104. DOI: 10.1063/1.3382344.

(58) Runge, E.; Gross, E. K. U. Density-Functional Theory for Time-Dependent Systems. *Physical Review Letters* **1984**, *52* (12), 997-1000. DOI: 10.1103/PhysRevLett.52.997.

(59) Petersilka, M.; Gossmann, U. J.; Gross, E. K. U. Excitation Energies from Time-Dependent Density-Functional Theory. *Physical Review Letters* **1996**, *76* (8), 1212-1215. DOI: 10.1103/PhysRevLett.76.1212.

(60) Heyd, J.; Scuseria, G. E.; Ernzerhof, M. Hybrid functionals based on a screened Coulomb potential. *The Journal of Chemical Physics* **2003**, *118* (18), 8207-8215. DOI: 10.1063/1.1564060.

(61) Liu, Z.; Wang, X.; Lu, T.; Yuan, A.; Yan, X. Potential optical molecular switch: Lithium@cyclo[18]carbon complex transforming between two stable configurations. *Carbon* **2022**, *187*, 78-85. DOI: https://doi.org/10.1016/j.carbon.2021.11.005.

(62) Lu, T.; Chen, F. Multiwfn: A multifunctional wavefunction analyzer. *Journal of Computational Chemistry* **2012**, *33* (5), 580-592. DOI: https://doi.org/10.1002/jcc.22885.

(63) Frisch, M.J.; Trucks, G. W.; Schlegel, H. B.; Scuseria, G. E.; Robb, M. A.; Cheeseman, J.R.; Scalmani, G.; Barone, V.; Petersson, G. A.; Nakatsuji, H.; et al. *Gaussian 16 Rev. C.01*; Wallingford, CT, 2016.

(64) Boys, S. F.; Bernardi, F. The calculation of small molecular interactions by the differences of separate total energies. Some procedures with reduced errors. *Molecular Physics* **1970**, *19* (4), 553-566. DOI: 10.1080/00268977000101561.

(65) Zou, Y.; Li, F.; Zhu, Z. H.; Zhao, M. W.; Xu, X. G.; Su, X. Y. An ab initio study on gas sensing properties of graphene and Si-doped graphene. *The European Physical Journal B* **2011**, *81* (4), 475-479. DOI: 10.1140/epjb/e2011-20225-8.

(66) Dai, J.; Yuan, J.; Giannozzi, P. Gas adsorption on graphene doped with B, N, Al, and S: A theoretical study. *Applied Physics Letters* **2009**, *95*, 232105. DOI: 10.1063/1.3272008 .

(67) Lu, Z.; Li, S.; Liu, C.; He, C.; Yang, X.; Ma, D.; Xu, G.; Yang, Z. Sulfur doped graphene as a promising metal-free electrocatalyst for oxygen reduction reaction: a DFT-D study. *RSC Advances* **2017**, *7* (33), 20398-20405, 10.1039/C7RA00632B. DOI: 10.1039/C7RA00632B.

(68) Shih, P.-H.; Do, T.-N.; Gumbs, G.; Lin, M.-F. Electronic and optical properties of doped graphene. *Physica E: Low-dimensional Systems and Nanostructures* **2020**, *118*, 113894. DOI: https://doi.org/10.1016/j.physe.2019.113894.

(69) Scharber, M. C.; Mühlbacher, D.; Koppe, M.; Denk, P.; Waldauf, C.; Heeger, A. J.; Brabec, C. J. Design Rules for Donors in Bulk-Heterojunction Solar Cells—Towards 10 % Energy-Conversion Efficiency. *Advanced Materials* **2006**, *18* (6), 789-794. DOI: https://doi.org/10.1002/adma.200501717.

(70) Perez, M. D.; Borek, C.; Forrest, S. R.; Thompson, M. E. Molecular and Morphological Influences on the Open Circuit Voltages of Organic Photovoltaic Devices. *Journal of the American Chemical Society* **2009**, *131* (26), 9281-9286. DOI: 10.1021/ja9007722.

(71) Willhelm, D.; Wilson, N.; Arroyave, R.; Qian, X.; Cagin, T.; Pachter, R.; Qian, X. Predicting Van der Waals Heterostructures by a Combined Machine Learning and Density Functional Theory

Approach. *ACS Applied Materials & Interfaces* **2022**, *14* (22), 25907-25919. DOI: 10.1021/acsami.2c04403.

(72) Scharber, M. C.; Sariciftci, N. S. Efficiency of bulk-heterojunction organic solar cells. *Progress in Polymer Science* **2013**, *38* (12), 1929-1940. DOI: https://doi.org/10.1016/j.progpolymsci.2013.05.001.

(73) Bernardi, M.; Palummo, M.; Grossman, J. C. Semiconducting Monolayer Materials as a Tunable Platform for Excitonic Solar Cells. *ACS Nano* **2012**, *6* (11), 10082-10089. DOI: 10.1021/nn303815z.

TOC Graphic

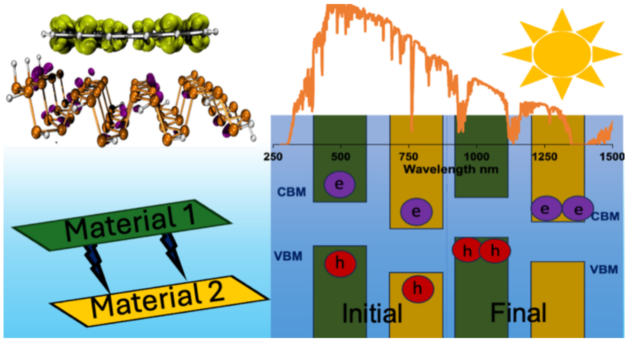
250
500
750
1000
1250
1500
Wavelength nm
CBM
VBM
e
h
Material 1
Material 2
Initial
Final
CBM
VBM